Experiments on flows in channels with spatially distributed heating

A. Inasawa[1,†], K. Taneda[1] and J. M. Floryan[2]

[1]Department of Aeronautics and Astronautics, Tokyo Metropolitan University, Asahigaoka 6-6, Hino, Tokyo 191-0065, Japan

[2]Department of Mechanical and Materials Engineering, University of Western Ontario, London, Ontario N6A 5B9, Canada

Flows in channels exposed to spatially distributed heating were investigated. Such flows are of interest as theoretical analyses suggest that heating leads to the reduction of pressure losses. A special apparatus providing the means for the creation of well-controlled spatially periodic heating with the desired intensity as well as precise control of the flow rate in flows with small Reynolds numbers was constructed. The apparatus works with air and provides optical access to the flow interior. The relevant theory has been generalized to handle the temperature fields measured in the experiments. The experiments were carried out for Reynolds numbers $Re < 20$ and at a single Rayleigh number based on the peak-to-peak temperature difference and channel half-height of $Ra_p = 3500$. Flow visualization and particle image velocimetry measurements demonstrated the formation of two-dimensional steady rolls whose size was dictated by Re, with the largest rolls observed for the smallest Re and the roll size being gradually reduced as Re increased until their complete elimination at the largest Re used in the experiment. An excellent agreement between the theoretically and experimentally determined complex flow fields was found. Wall shear stresses extracted from the velocity measurements agree with their theoretical counterparts within the expected accuracy. The agreement between the experimental and theoretical velocity fields and their unique relation with the corresponding pressure fields indirectly verify the heating-induced pressure-gradient-reducing effect.

Key words: drag reduction

1. Introduction

The increased cost of energy and the environmental impact of its use have resulted in a renewed interest in the search for drag reduction techniques. Drag results from motion-induced changes in the pressure field and from friction between fluid and bounding surfaces, with the former typically subdivided into the form drag and the interaction drag (Mohammadi & Floryan 2012). The form drag is created by the asymmetry of the pressure field between the upstream and downstream sides of a moving object and its origins are well understood. The interaction drag results from

† Email address for correspondence: ainasawa@tmu.ac.jp

the projection of the pressure field onto the surface topography and its origins are poorly understood. The mechanisms responsible for the shear drag are well understood and this analysis focused on the development of techniques suitable for its reduction.

The magnitude of wall shear is proportional to the fluid viscosity and the wall-normal velocity gradient. If the fluid type cannot be altered, shear can be reduced only by altering the character of the fluid motion near the wall. Modifications of either the laminar or turbulent flows lead to a direct change of the shear with the expectation that the modified flow produces less friction. The indirect change involves delay of the laminar–turbulent transition as the laminar shear is always smaller than the turbulent shear. The latter approach has been explored primarily in the context of the development of laminar flow airfoils (Arnal, Perraud & Séraudie 2008). The desired flow changes can be created using either passive or active means. Surface topography (Ou, Perot & Rothstein 2004), surface transpiration (Min *et al.* 2006; Bewley 2009; Hœpffner & Fukagata 2009; Mamori, Iwamoto & Marata 2014) and plasma- (Inasawa, Ninomiya & Asai 2013), sound- (Kato, Fukunishi & Kobayashi 1997) or piezo-driven actuators (Fukunishi & Ebina 2001) represent commonly used techniques. Biological systems provide additional intriguing directions for further developments as natural evolution must have led to their optimization (Martin & Bhushan 2014).

Reduction of laminar shear drag is the focus of the present work. One of the ways to achieve this goal is the development of appropriate surface topography. If a smooth surface is viewed as the reference case, all its alterations will increase the wetted area and, thus, the reduction of the wall shear must be large enough so as to overcome the potential drag increase due to the increase of this area. It is known that longitudinal grooves (grooves parallel to the flow direction) can lead to a significant drag reduction through changes in the distribution of the bulk flow (Szumbarski, Blonski & Kowalewski 2011; Mohammadi & Floryan 2013*a*, 2014, 2015; Moradi & Floryan 2013; Raayai-Ardakani & McKinley 2017; Yadav, Gepner & Szumbarski 2017, 2018). The grooves can be optimized (Mohammadi & Floryan 2013*b*) with their most effective forms depending on the constraints used. In the case of grooves of equal height and depth, the optimal shape has the form of a golden trapezoid, while in the case of grooves with different depth and height the shape is well approximated by the Gaussian function. The grooves are effective only if the flow remains laminar and the required estimates of stability limits are available (Szumbarski 2007; Moradi & Floryan 2014; Mohammadi, Moradi & Floryan 2015; Yadav *et al.* 2017, 2018).

The second group of techniques relies on the so-called super-hydrophobic effect (Rothstein 2010) and is limited to applications in moving liquids. The essence of this effect is the ability of surface topography to trap gas bubbles in micropores. The direct contact between liquid and solid is partially replaced by the contact between liquid and gas, reducing the shear stress acting on the liquid. This effect is counteracted by the simultaneous creation of pressure drag by surface irregularities. Experimental evidence shows that it is possible nevertheless to create systems with overall drag reduction (Ou *et al.* 2004; Ou & Rothstein 2005; Joseph *et al.* 2006; Truesdell *et al.* 2006; Park, Park & Kim 2013; Park, Sun & Kim 2014; Srinivasan *et al.* 2013). The effectiveness of this method can be increased by reshaping the surface pores (Samaha, Tafreshi & Gad-El-Hak 2011) and by increasing hydrophobicity through changes in the surface chemistry (Quéré 2008; Reyssat, Yeomans & Quéré 2008; Zhou *et al.* 2011). The stability characteristics of flows over super-hydrophobic surfaces are yet to be established, including conditions which guarantee the existence of laminar flows.

Other system limitations are associated with the integrity of the gas–liquid interface, which depends on the surface tension and shear-driven interfacial instabilities, and on the hydrostatic pressure which can lead to the collapse of gas bubbles leaving liquid directly exposed to rough surface (Poetes *et al.* 2010; Bocquet & Lauga 2011; Samaha, Tafreshi & Gad-El Hak 2012; Aljallis *et al.* 2013).

Bubble collapse can be avoided by working with two liquids leading to the concept of liquid-infused surfaces (Wong *et al.* 2011). The infusing liquid has much higher viscosity than the gas, but drag reduction is nevertheless possible (Rosenberg *et al.* 2016; Solomon, Khalil & Varanasi 2014, 2016). Substantial drag reduction has been reported recently (Van Buren & Smits 2017). This technique is subject to limitations associated with variations of pressure along the surface which causes migration of infusing liquid.

The third group of methods relies on the use of spatial heating patterns leading to the formation of convection rolls. The fluid rotation inside the rolls is driven by horizontal density gradients and, thus, provides a propulsive force assisting fluid movement. The rolls isolate the stream from direct contact with the bounding walls reducing friction opposing fluid movement. This effect, sometimes referred to as the super-thermohydrophobic effect (Floryan 2012), operates in single-phase fluids, is independent of the surface topography and, thus, offers advantages over the super-hydrophobic effect. The net result is difficult to predict as the stream needs to meander between convection rolls potentially increasing friction. The heat transfer consequences of such an arrangement have been discussed in Hossain & Floryan (2013*a*). The strength of this effect is increased by combining spatially distributed and uniform heating (Floryan & Floryan 2015), and by periodically heating both walls with the proper phase difference between the upper and lower heating patterns (Hossain & Floryan 2016). The effect is resilient as it can be generated by heating applied at either the lower or upper wall (Hossain & Floryan 2014). The flow must remain laminar for the method to work and the relevant stability characteristics are available (Hossain & Floryan 2015*a*). The method remains effective for small Reynolds numbers (Hossain, Floryan & Floryan 2012) as stronger flows eliminate convection bubbles. It can also be used to reduce forces between plates in relative motion (Floryan, Shadman & Hossain 2018).

The main objective of this study is to analyse experimentally flows in channels exposed to spatially distributed heating, to confirm their theoretically predicted properties including the structure of the velocity field and to examine if such flows can bring about a reduction of pressure losses. Section 2 presents the model problem generalized to arbitrary but spatially periodic heating such as that found in experiments. In this model, the lower wall is heated in a periodic manner while the upper wall is isothermal. This same section provides a description of the numerical algorithm used to solve the field equations. Section 3 provides a description of the specially constructed experimental apparatus as well as the measurement procedures. Section 4 provides a discussion of the results including comparisons of numerical and experimental data. Section 5 presents a short summary of the main conclusions.

2. Problem formulation

Consider the steady, two-dimensional flow of a fluid confined in a channel bounded by two parallel walls extending to $\pm\infty$ in the x-direction and driven by a pressure gradient (see figure 1). The gravitational acceleration g^* is acting in the negative y-direction, the fluid is incompressible, Newtonian, and has thermal conductivity k^*,
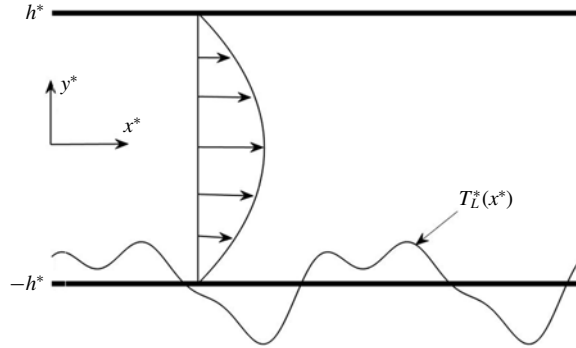
FIGURE 1. Schematic diagram of the flow system.

specific heat c^*, thermal diffusivity $\kappa^* = k^*/\rho^* c^*$, kinematic viscosity ν^*, dynamic viscosity μ^* and thermal expansion coefficient Γ^* and variations of the density ρ^* follow the Boussinesq approximation. Here asterisks denote dimensional quantities. The velocity field, pressure field and flow rate in the isothermal channel have the form

$$\boldsymbol{v}_0(x, y) = [u_0(y), 0] = [1 - y^2, 0], \quad p_0(x, y) = -2x/Re, \quad Q_0 = 4/3, \quad (2.1a\text{--}c)$$

where the channel half-height h^* has been used as the length scale, $\boldsymbol{v}_0(x, y) = [u_0, v_0]$ denotes the velocity vector scaled with the maximum of the x-velocity U_{max}^*, p_0 stands for the pressure scaled with $\rho^* U_{max}^{*2}$ and the Reynolds number is defined as $Re = U_{max}^* h^*/\nu^*$.

The lower wall is heated resulting in its temperature T_L^* varying periodically in x^* with wavelength $\lambda^* = 2\pi/\alpha^*$, where α^* is the wavenumber, while the upper wall is isothermal and kept at temperature T_U^*. We define the relative temperature $\theta^* = T^* - T_U^*$, resulting in boundary temperatures of the form

$$\theta_L^*(x^*) = \theta_{uni}^* + \theta_p^* \sum_{n=-\infty, n\neq 0}^{n=+\infty} [\theta_p^{(n)*}/\theta_p^*] e^{in\alpha^* x^*}, \quad \theta_U(x^*) = 0, \quad (2.2a,b)$$

where L and U refer to the lower and upper walls, respectively, $\theta_{uni}^* = T_{mean,L}^* - T_U^*$, θ_p^* is the difference between the maximum and minimum of the lower-wall temperature and $\theta_p^{(n)*}$ are the complex amplitudes of the Fourier modes required to describe spatial temperature variations. These amplitudes satisfy the reality condition, which requires that $\theta_p^{(n)*}$ and $\theta_p^{(-n)*}$ are complex conjugates. Use of $\kappa^* \nu^*/(g^* \Gamma^* h^{*3})$ as the temperature scale results in the following dimensionless expressions for the wall temperatures:

$$\theta_L(x) = Ra_{uni} + Ra_p \sum_{n=-\infty, n\neq 0}^{n=+\infty} \theta_p^{(n)} e^{in\alpha x}, \quad \theta_U(x) = 0, \quad (2.3a,b)$$

where $Ra_{uni} = g^* \Gamma^* h^{*3} \theta_{uni}^*/(\kappa^* \nu^*)$ and $Ra_p = g^* \Gamma^* h^{*3} \theta_p^*/(\kappa^* \nu^*)$ are the uniform and periodic Rayleigh numbers. All material properties used in these expressions are to be evaluated at the upper-wall temperature T_U^*.

The flow in the heated channel is described by the continuity, Navier–Stokes and energy equations of the form

$$\frac{\partial u}{\partial x} + \frac{\partial v}{\partial y} = 0, \quad u\frac{\partial u}{\partial x} + v\frac{\partial u}{\partial y} = -\frac{\partial p}{\partial x} + \nabla^2 u, \quad (2.4a,b)$$

$$u\frac{\partial v}{\partial x} + v\frac{\partial v}{\partial y} = -\frac{\partial p}{\partial y} + \nabla^2 v + Pr^{-1}\theta, \quad u\frac{\partial \theta}{\partial x} + v\frac{\partial \theta}{\partial y} = Pr^{-1}\nabla^2\theta, \quad (2.4c,d)$$

where (u, v) are the velocity components in the (x, y) directions, respectively, scaled with $U_v^* = v^*/h^*$ as the velocity scale, p stands for the pressure scaled with $\rho^* U_v^{*2}$ as the pressure scale and $Pr = v^*/\kappa^*$ is the Prandtl number. The relevant boundary conditions have the form

$$u(x, -1) = u(x, 1) = 0, \quad v(x, -1) = v(x, 1) = 0, \quad \theta(x, -1) = \theta_L(x), \quad \theta(x, 1) = 0. \quad (2.5a-d)$$

The relation between the heating and the pressure losses is quantified by comparing pressure gradients required to drive the same flow rate through the isothermal and heated channels. This gradient in the case of the heated channel can be written as

$$\left.\frac{\partial p}{\partial x}\right|_{mean} = Re(-2 + A/Re), \quad (2.6)$$

where a positive value of the correction A identifies reduction of pressure losses. To make this comparison meaningful, one must impose the fixed flow rate constraint of the form

$$Q = \int_{-1}^{1} u \, dy = \frac{4}{3} Re \quad (2.7)$$

on the solution of the flow problem.

System (2.3)–(2.6) can be expressed in terms of the stream function defined in the usual manner, i.e. $u = \partial\psi/\partial y$, $v = -\partial\psi/\partial x$, and normalized with condition $\psi(-1) = 0$, resulting in a problem of the form

$$\nabla^4\psi - Pr^{-1}\frac{\partial\theta}{\partial x} = N_{VV}, \quad \nabla^2\theta = Pr\, N_{V\theta}, \quad (2.8a,b)$$

$$\psi(x, -1) = 0, \quad \psi(x, 1) = \frac{4}{3}Re, \quad \left.\frac{\partial\psi}{\partial y}\right|_{(x,y=\pm1)} = 0, \quad \theta(x, -1) = \theta_L(x), \quad \theta(x, 1) = 0, \quad (2.8c-g)$$

where the nonlinear terms N_{VV} and $N_{V\theta}$ have the following definitions:

$$N_{VV} = \frac{\partial}{\partial y}\left(\frac{\partial}{\partial x}\widehat{uu} + \frac{\partial}{\partial y}\widehat{uv}\right) - \frac{\partial}{\partial x}\left(\frac{\partial}{\partial x}\widehat{uv} + \frac{\partial}{\partial y}\widehat{vv}\right), \quad N_{V\theta} = \frac{\partial}{\partial x}\widehat{u\theta} + \frac{\partial}{\partial y}\widehat{v\theta}, \quad (2.9a,b)$$

with symbol $\widehat{ab}$ denoting a product of functions a and b. The x-dependence of the flow quantities is captured by expressing them as Fourier expansions of the form

$$\psi(x, y) = \sum_{n=-\infty}^{n=+\infty} \varphi^{(n)}(y)e^{in\alpha x}, \quad u(x, y) = \sum_{n=-\infty}^{n=+\infty} u^{(n)}(y)e^{in\alpha x}, \quad v(x, y) = \sum_{n=-\infty}^{n=+\infty} v^{(n)}(y)e^{in\alpha x}, \quad (2.10a-c)$$

$$\theta(x, y) = \sum_{n=-\infty}^{n=+\infty} \emptyset^{(n)}(y)e^{in\alpha x}, \quad p(x, y) = Ax + \sum_{n=-\infty,}^{n=+\infty} p^{(n)}(y)e^{in\alpha x}, \quad (2.10d,e)$$

$$N_{VV}(x, y) = \sum_{n=-\infty}^{n=+\infty} N_{VV}^{(n)}(y)e^{in\alpha x}, \quad N_{V\theta}(x, y) = \sum_{n=-\infty}^{n=+\infty} N_{V\theta}^{(n)}(y)e^{in\alpha x} \quad (2.10f,g)$$

subject to a proper truncation. These expansions are substituted into the field equations and the Fourier modes are separated leading to a system of ordinary differential equations for the modal functions. This system is solved using the Chebyshev collocation method (Hossain & Floryan 2015*a*,*b*). As a part of the verification process, the same system is solved using the variable-step-size finite-difference approximation (Hossain & Floryan 2013*b*). The numerical parameters were adjusted during the codes' calibration stage to guarantee at least six-digit agreement between both methods. Use of 30 Fourier modes and 51 Chebyshev polynomials is sufficient in the former case. The same number of Fourier modes is used in the latter case while the error in the solution of the modal equations is controlled through automatic selection of the number and distribution of grid points to meet the prescribed error bounds. The pressure field, with the exception of the pressure gradient correction A, is determined as a part of the post-processing by substituting the calculated velocity components into the momentum equations and solving them for the pressure modal functions.

The mean horizontal pressure gradient is required to overcome frictional resistance. The shear stresses as well as the shear forces per unit length and width of the channel acting on the fluid at the walls have the forms

$$\tau_L = -\left.\frac{\mathrm{d}u}{\mathrm{d}y}\right|_{y=-1}, \quad \tau_U = \left.\frac{\mathrm{d}u}{\mathrm{d}y}\right|_{y=1}, \quad F_L = \lambda^{-1}\int_0^\lambda \tau_L\,\mathrm{d}x, \quad F_U = \lambda^{-1}\int_0^\lambda \tau_U\,\mathrm{d}x, \quad (2.11a\text{--}d)$$

where τ stands for the shear stress scaled with $\rho^* U_v^{*2}$, F stands for the shear force scaled in the same manner and subscripts U and L refer to the upper and lower walls, respectively. The shear and pressure forces must balance each other, i.e.

$$(F_L + F_U) = 2\left.\frac{\partial p}{\partial x}\right|_{mean}. \tag{2.12}$$

It remains to be determined if heating leads to a reduction of the mean pressure gradient or, in other words, a reduction of the mean shear stress.

3. Experimental set-up and procedure

A special experimental facility using air as the working medium (see figure 2) was developed to investigate heating effects. The test rig has the form of a 3 m long rectangular channel with a height of $2h^* = 20$ mm and width $s^* = 420$ mm giving a cross-sectional aspect ratio of $s^*/(2h^*) = 21$. The channel is tall enough to provide optical access required for non-intrusive velocity measurements. A Cartesian reference system consisting of the streamwise x-, transverse y- and spanwise z-coordinates with the origin at the middle of the channel at the x-location corresponding to the middle of the first heating element is used to describe the system geometry. The channel is mounted horizontally using a laser level. The flow is driven by a piston installed upstream of the test section whose motion is controlled using a ball screw driven by a servo-motor. The speed of the piston can be adjusted digitally, permitting reaching the target velocity with an accuracy of 0.41 %.

The piston creates a plug flow with a well-defined mass flow rate which is then converted through viscous friction into fully developed Poiseuille flow downstream from the piston. Formation of Poiseuille flow is analogous to that found in the channel entrance flow problem. It is known that the entry length is minimal for low-*Re* flows
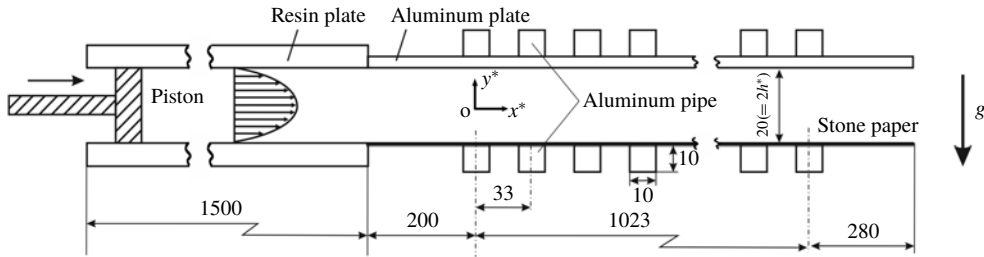
FIGURE 2. Sketch of the experimental apparatus (all dimensions are in mm).
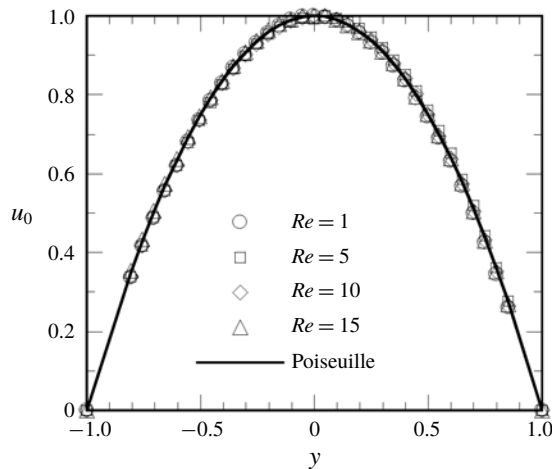

FIGURE 3. Streamwise velocity profiles in the isothermal channel at $x = 75$, $z = 0$.

(Sadri & Floryan 2002a,b; Asai & Floryan 2004). The proper establishment of Poiseuille flow has been verified experimentally using the test facility with heating turned off, as illustrated in figure 3. The maximum (centre) velocity was found to be $U_{max}^{*} = 1.6, 3.3, 4.9, 8.1, 11.4, 16.3, 24.4$ mm s^{-1} at $Re = 1, 2, 3, 5, 7, 10, 15$, respectively.

The lower wall is equipped with a set of transverse aluminium pipes carrying hot and cold water coming from baths whose temperatures can be controlled with a resolution of 0.1 K. These pipes are covered with 0.2 mm thick stone paper and provide means for the establishment of a streamwise-periodic temperature distribution at the surface. The wavelength of temperature variations is $\lambda^{*} = 66$ mm, giving a wavenumber $\alpha = 2\pi h^{*}/\lambda^{*} = 0.95$. A total of 16 heating periods was used, with most of the observations made around the 11th period ($70 \leqslant x \leqslant 81$). The upper wall was made of 5 mm thick aluminium plate with transverse aluminium pipes carrying water of a specified temperature attached to its external surface providing means for maintaining isothermal conditions. The apparatus creates a two-dimensional x-periodic temperature of the lower wall as illustrated in figures 4 and 5, with the spanwise temperature variations being within ± 0.5 K at $x = 72.6$.

The lower-surface temperature was measured using an infrared thermal imaging camera (Nippon Avionics H2640). Its temperature was also monitored during experiments using sheet-form thermocouples (Chino C060, Type T). Velocity
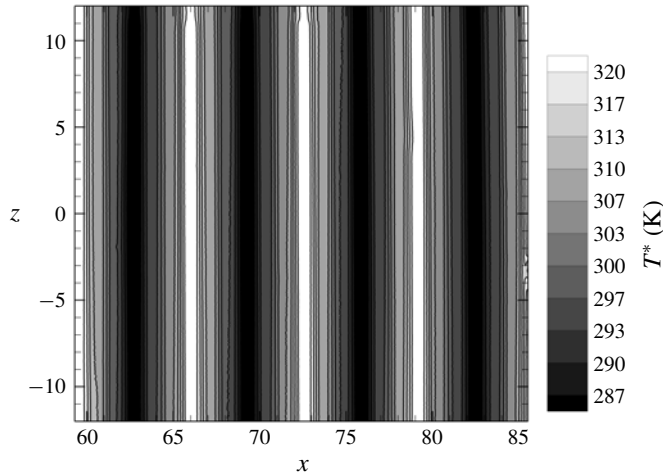
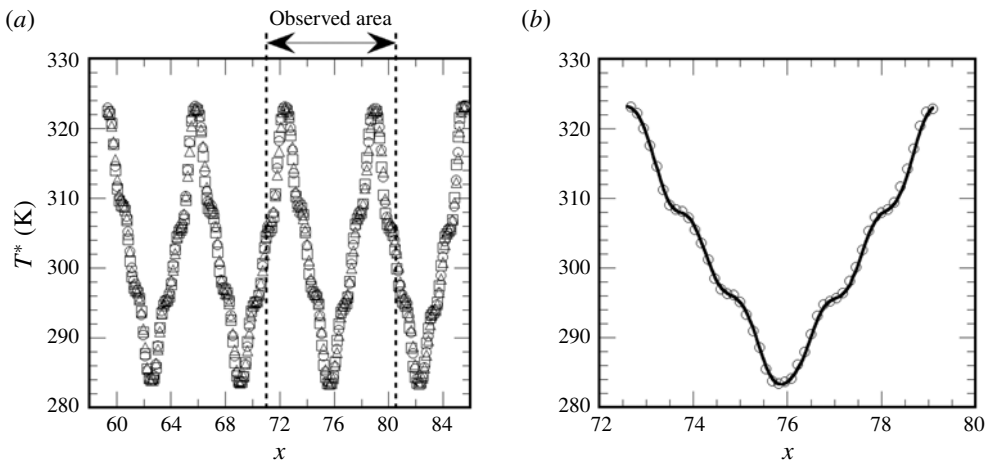FIGURE 4. Contour map of the lower-wall temperature for $Ra_p = 3500$.

FIGURE 5. Streamwise variations of the bottom-wall temperature for $Ra_p = 3500$. (*a*) Experimental data for three spanwise locations ($\bigcirc$, $z = 0$; $\square$, $z = 10$; $\triangle$, $z = -10$). (*b*) Temperature distribution at $72.6 \leqslant x \leqslant 79.2$ and $z = 0$, and its Fourier representation ($\bigcirc$, experiments; solid line, Fourier representation).

measurements were carried out using a particle image velocimetry (PIV) system (Dantec Dynamic Studio) consisting of a double-pulsed Nd:YAG laser (Quantel Ever Green) and a CCD camera with a resolution of 2048×2048 pixels (Dantec FlowSense EO 4M). A laser light sheet with a thickness of approximately 1 mm was used to illuminate 1 µm diameter seeding in the (x, y)-plane. The photographed area had a size of $(x^*, y^*) = (100 \text{ mm}, 25 \text{ mm})$. The least squares matching algorithm was employed in post-processing. The interrogation size and overlap in the y-direction were $(x, y) = (33, 22)$ pixels and 50 %, respectively, giving $(37, 37)$ velocity vectors in the (x, y)-directions per one period of heating.

   In order to determine the sample size N necessary to achieve statistical convergence, preliminary measurements were made for an isothermal channel using different sample

n	1	2	3	4	5	6	7	8	9	10
Real ($\theta_p^{(n)}$)	0.2048	0.0074	0.0326	0.0004	0.0209	−0.0005	−0.0077	−0.0008	0.0001	−0.0001
Imag ($\theta_p^{(n)}$)	−0.0077	0.0046	0.0033	−0.0026	−0.0007	0.0003	−0.0001	0	0.0005	−0.0011

TABLE 1. Fourier coefficients of expansion (2.3) corresponding to the experimental conditions.

sizes in the range of $10 \leqslant N \leqslant 100$ (see figure 3). It was found that the velocity profiles were independent of the sample size and the flow rate was within 1 % of the theoretical value of $Q/Re = 4/3$ for $N \geqslant 30$. Thus, $N = 50$ was employed in the experiment. The uncertainty of velocity measurements was estimated for each step of the measurement sequence. The accuracy of PIV is limited by several factors, e.g. particle response to fluid motion, position of light sheet, jitter associated with camera and laser response to controlling pulse, distortion of lens and image sensor, size of the interrogation area and image-matching algorithm. The biased error is estimated to be about 0.1 pixels, which is 5 % of typical particle displacement (2 pixels). However, the excellent agreement for the isothermal flow suggests that the biased error in the instrumentation used is smaller than that. The random uncertainty is mainly due to scatter of the measured velocity resulting from particle distribution and/or flow conditions. When we use a 95 % confidence interval, the value of the time-averaged mean streamwise velocity $\overline{u^*}$ is within the interval of $\overline{u^*} \pm 1.96(\sqrt{s_{u^*}/N})$, where s_{u^*} is the variance of u^*. The relative uncertainties were found to be about ± 1 % of $\overline{u^*}$ for all measurements which approximately correspond to the size of plotted symbols.

4. Discussion of results

In the experiments reported in this paper, the cold/hot water supplies were adjusted to keep the upper wall at a constant temperature $T_U^* = 303.2$ K, a constant peak-to-peak amplitude of temperature variations along the bottom wall at $\theta_p^* = 39.8$ K and mean temperature at $T_{mean,L}^* = 302.8$ K. Since matching of the mean temperature of the lower wall with the temperature of the upper wall was difficult, the experiments were carried out with the mean temperature of the bottom wall lower than the temperature of the upper wall giving $\theta_{uni}^* = T_{mean,L}^* - T_U^* = -0.4$ K. This arrangement resulted in a periodic Rayleigh number of $Ra_p = 3500$ and a uniform Rayleigh number of $Ra_{uni} = -35$. In the following discussion, the temperature maxima and minima are referred to as hot and cold spots, respectively. It was sufficient to use the first 10 modes in (2.3) to describe the streamwise variations of the bottom-wall temperature (see figure 5b). The corresponding Fourier expansion coefficients are given in table 1.

Fluid movement results from an interaction/competition between two types of forces, i.e. the externally imposed horizontal pressure gradient and the buoyancy forces. The resulting flow topologies change significantly depending on the relative magnitudes of these forces, as illustrated in figure 6, which displays both experimental and theoretical results. In this figure, the hot spots are always located at $x = 72.6$ and 79.2, and the cold spot at $x = 75.9$.

In the case of $Re = 0$, the fluid movement is driven only by buoyancy forces, resulting in a topology consisting of counter-rotating rolls with the fluid moving upwards above the hot spots and downwards above the cold spots (see figure 6a). The upward movement of the warm plumes is stronger than the downward movement of the cold plumes resulting in the roll centres being attracted towards the hot spots.
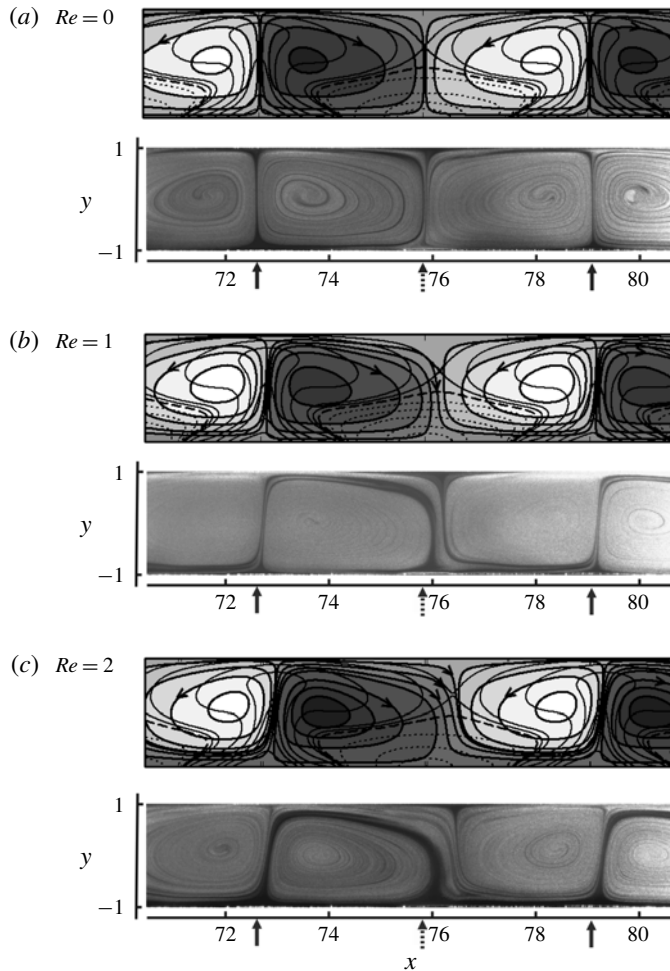
FIGURE 6. For caption see page 12.

Heating rather than cooling dominates as the fluid temperature throughout most of the flow domain increases above the mean lower-wall temperature, except in a small zone around the cold spot where the temperature dips below the mean temperature.

A piston forces the fluid to move in the positive x-direction with the flow rate and the Reynolds number dictated by the piston velocity. The velocity field has a typical Poiseuille form upstream of the heated section, as illustrated in figure 3. Figure 6(b) displays the flow topology resulting from the Poiseuille flow with $Re = 1$ exposed to heating. One can look at this flow field as resulting from the convection field shown in figure 6(a) modified by the horizontal pressure gradient. The rolls persist in the same locations trapping in their interiors a certain volume of fluid while the remaining fluid, which is pushed to the right by the piston, finds its way through a well-defined stream tube which meanders around the rolls, moving upwards above the hot spots and downwards above the cold spots. The position of the stream tube is kinematically consistent with the rolls' rotation. The question of interest is whether the pressure gradient required to generate this particular flow rate is larger or smaller than in the isothermal case. The contact between the stream tube and the walls has been
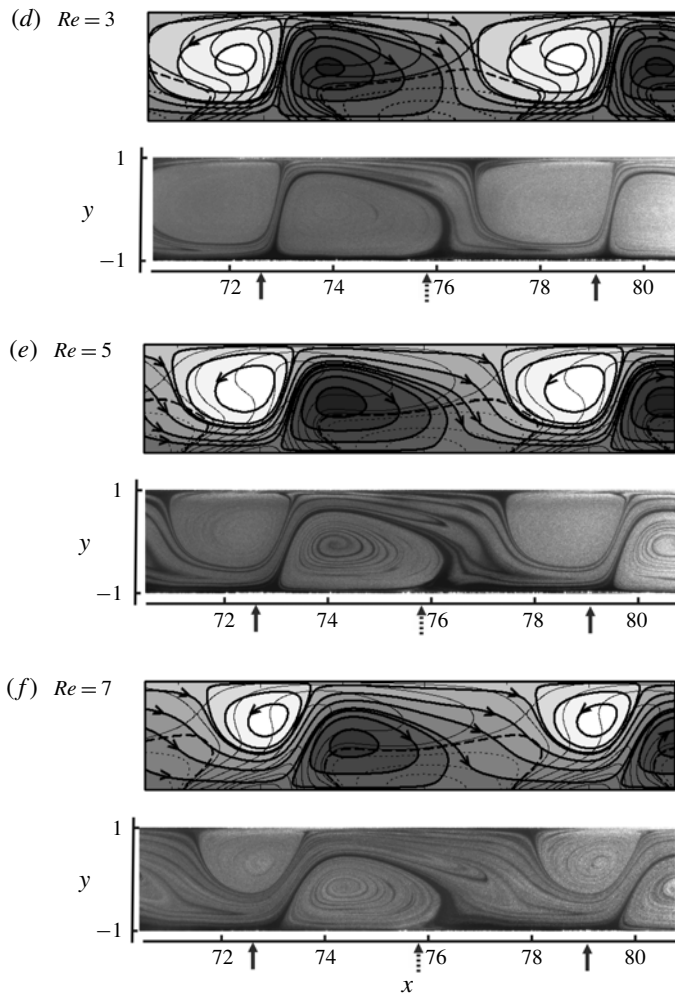
FIGURE 6 (cntd). For caption see next page.

largely eliminated which suggests potential reduction of pressure losses, similar to the case of the super-hydrophobic effect (Rothstein 2010), and this has led to referring to this effect as the super-thermohydrophobic effect (Floryan 2012). The rolls act as 'bearings' carrying the stream tube and this should lead to a further reduction of the pressure gradient. The bearings' rotation is partially driven by the buoyancy force, which should contribute to the reduction of pressure losses, and partially by the shear between the fluid in the stream tube and in the rolls, which should increase the pressure losses. The complex form of the stream tube as well as its length suggests the formation of high shear forces which would increase the drag. The rolls reduce the cross-sectional area available to the flow and this should increase pressure losses. Since all these effects are simultaneously present and oppose each other, determining whether the drag decreases or increases requires detailed analysis. Before proceeding with the rest of the discussion, we point out an excellent agreement between the theoretically and experimentally determined flow fields (see figure 6).

An increase of the horizontal mean pressure gradient while keeping the same heating conditions (the same buoyancy forces) results in an increase of the horizontal
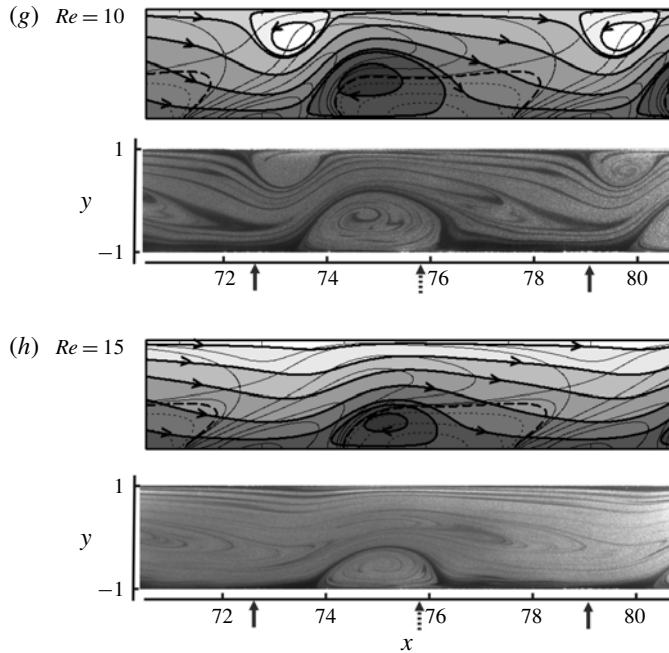
FIGURE 6 (cntd).   Comparisons of the theoretical (upper panels) and experimental (lower panels) flow fields for $Re = $ (*a*) 0, (*b*) 1, (*c*) 2, (*d*) 3, (*e*) 5, (*f*) 7, (*g*) 10, (*h*) 15. Locations of the hot spots ($x = 72.6$ and 79.2) are identified using solid arrows while location of the cold spot ($x = 75.9$) is identified using dotted arrows. Shading in the experimental panels results from smoke visualization. Shading in the theoretical panels changes from the local minimum (darkest) to the local maximum (lightest) of the stream function. For the theoretical results, the thick solid lines represent streamlines, the thin solid lines represent the positive isotherms while the thin dotted lines represent the negative isotherms. For $Re = 0$, 1, the plotted isotherms correspond to $\theta/\theta_{max} = -0.65, -0.45, -0.2, -0.1, 0, 0.01, 0.02, 0.04, 0.1, 0.2, 0.3, 0.5, 0.8$; for $Re = 2$, 3, $\theta/\theta_{max} = -0.97, -0.65, -0.33, -0.1, 0, 0.02, 0.04, 0.1, 0.2, 0.3, 0.4, 0.65$; for $Re = 5$, 7, $\theta/\theta_{max} = -0.45, -0.2, -0.06, 0, 0.01, 0.04, 0.1, 0.2, 0.3, 0.4, 0.55, 0.8$; for $Re = 10$, $\theta/\theta_{max} = -0.45, -0.2, -0.06, 0, 0.01, 0.013, 0.06, 0.1, 0.2, 0.3, 0.4, 0.8$; for $Re = 15$, $\theta/\theta_{max} = -0.45, -0.2, -0.06, 0, 0.01, 0.02, 0.06, 0.1, 0.2, 0.3, 0.8$. The thick dashed lines identify isotherms corresponding to $\theta = 0$.

flow rate and increase of the Reynolds number. Results for $Re = 2$ displayed in figure 6(*c*) demonstrate the existence of a flow topology qualitatively similar to that for $Re = 1$ but with the stream tube becoming wider and straighter as it has to carry a larger flow rate. This process is continued at $Re = 3$ (figure 6*d*) with the size of the upper rolls decreasing faster than that of the lower rolls. The change in the character of the temperature field is first noticed for $Re = 5$ with the colder region extending further in the downstream direction (see figure 6*e*). At $Re = 10$ (figure 6*g*) the upper rolls become marginal and the stream tube occupies most of the channel. At $Re = 15$ (figure 6*h*), the upper rolls have been eliminated while the lower rolls still exist in a residual form. Further increase of Re eliminates the rolls altogether with the flow topology becoming identical to that found in an isothermal channel (details not shown). The pressure-gradient-driven flow becomes so strong that the buoyancy
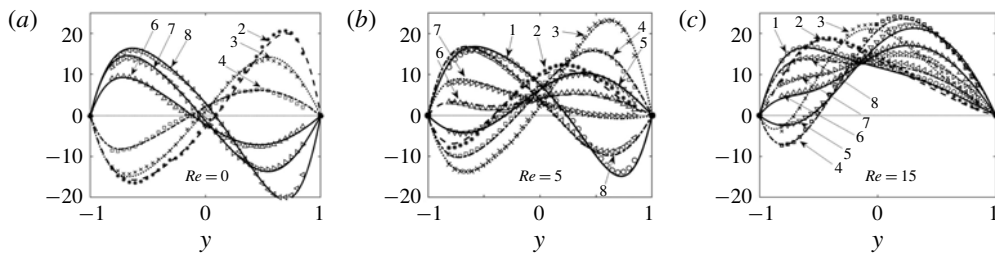
FIGURE 7. Distributions of the horizontal velocity component every 1/8 of the heating wavelength starting at the hot spot (location 1) for $Re = 0$ (a), $Re = 5$ (b) and $Re = 15$ (c). Locations 1, 2, 3, ..., 8 correspond to $x/\lambda = 0$, 1/8, 1/4, 3/8, 1/2, 5/8, 6/8, 7/8, respectively, where $x = 0$ corresponds to the left-hand hot spot in the observation area. Locations 1 and 5 are not shown in (a) as they correspond to the flow moving only in the vertical direction. Symbols identify experimental points while solid lines illustrate theoretical results.

forces no longer play any role in the fluid movement. In closing this part of the discussion, one should note the downstream movement of the separation point at the lower wall where the stream tube turns upwards; this point moves from $x = 72.6$, which represents the limit for $Re \rightarrow 0$ (no pressure gradient effects), to $x \approx 74$ at $Re = 15$ (buoyancy effects are negligible).

It is known that thermal convection flows are highly unstable and tend to break into secondary motions. Results presented in figure 6 demonstrate that the flow is stationary and stable under the conditions used in the experiment and remains two-dimensional. The critical Rayleigh number for the onset of secondary convective motion for unimodal periodic heating is $Ra_p \approx 3000$ (Hossain & Floryan 2015b). Its value rises rapidly when the lower-wall mean temperature decreases below the upper-wall temperature ($Ra_{uni} < 0$; Hossain & Floryan 2017) as is the case in the present experiment. Stability conditions in the case of multimodal heating remain to be determined but, as the current results demonstrate, the flow remains stable at $Ra_p = 3500$.

Measurements of the horizontal velocity component were carried out using the non-intrusive PIV technique. It is known that the measurements near the walls are biased due to low-density inhomogeneous seeding, reflection of mirrored images and other technical challenges, as discussed by Kahler, Scharonowski & Cierpka (2012). Ideally, the bias errors may be averaged out when the velocity gradient is constant, and particles are seeded homogeneously. In the present flow configuration, however, velocity gradients change drastically in the near-wall region. In addition, the magnitude of the velocity changes significantly as a function of x as u decreases significantly in locations where the vertical roll motion dominates (see figure 6). Results displayed in figure 7 for three illustrative cases, i.e. $Re = 0$, 5 and 15, demonstrate a very good agreement between experimental and theoretical results in the bulk of the flow as well as a reduction of the backward flow as Re increases. The lack of experimental points in the immediate neighbourhoods of the walls is associated with the limitations of the measurement technique.

Solutions of the field equations for the heating conditions used in the experiment demonstrate that reduction of pressure losses does occur (see figure 8). The magnitude of the drag reduction is determined by the interplay between the buoyancy forces and the externally imposed horizontal pressure forces. The shift from the former
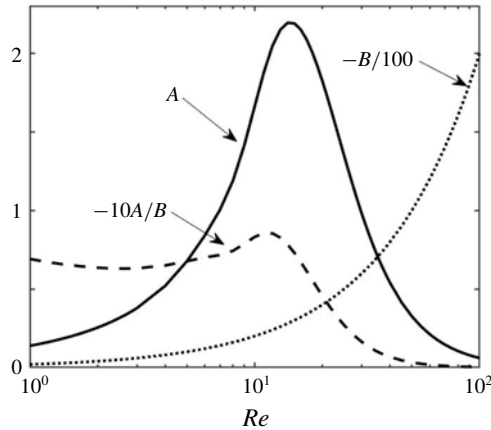
FIGURE 8. Variations of the pressure gradient correction (A), the pressure gradient for the isothermal channel ($B = -2 \times Re$) and the ratio A/B as functions of the flow Reynolds number.

Re	1	2	3	5	7	10	15
$\partial p/\partial x\vert_{iso}$ (Pa m^{-1})	0.605×10^{-3}	1.21×10^{-3}	1.815×10^{-3}	3.025×10^{-3}	4.235×10^{-3}	6.05×10^{-3}	9.075×10^{-3}
$\tau_{L,iso} = \tau_{U,iso}$	-2	-4	-6	-10	-14	-20	-30
$\tau_{L,mean}$	-0.679	-1.353	-2.05	-3.568	-5.676	-11.198	-23.463
$\tau_{U,mean}$	-3.045	-6.14	-9.194	-15.079	-20.032	-25.447	-32.159
A	0.138	0.254	0.379	0.677	1.002	1.662	2.189
Reduction (%)	6.9	6.34	6.3	6.76	8.19	8.39	7.3

TABLE 2. Variations of the theoretically determined isothermal mean pressure gradient ($\partial p/\partial x\vert_{iso}$), isothermal mean shear at the upper ($\tau_{U,iso}$) and lower ($\tau_{U,iso}$) walls, mean shear at the lower wall ($\tau_{L,mean}$), mean shear at the upper wall ($\tau_{U,mean}$), the pressure gradient correction (A) and the same correction expressed as a fraction of the isothermal pressure loss for the Reynolds numbers used in the experiments.

dominating flow at small Re to the latter dominating flow at larger Re takes place at $Re \approx 14$. The highest reduction in relative terms is achieved at $Re = 11$ and it is about 8.5 %. The elimination of the drag-reducing effect for larger Re correlates well with the elimination of convection bubbles. The magnitudes of pressure gradients are extremely small (see table 2) and, thus, the heating-induced changes in pressure drops over the length of the experimental model are not accessible to direct measurements. This necessitates the use of an indirect method.

The pressure gradient can be determined from a balance of forces acting on a convenient control volume, i.e. (2.12). Since pressure losses are generated only by wall shear, measurements of shear over one heating wavelength should provide information sufficient for determination of the pressure gradient. The theoretical shear distributions between two adjacent hot spots determined for the experimental conditions are displayed in figure 9. Shear at the lower wall changes direction depending on the position with respect to the convection bubbles. It acts in the positive x-direction in the zone adjacent to the clockwise-rotating bubble and, thus, assists with the fluid movement along the channel, and in the opposite direction in the
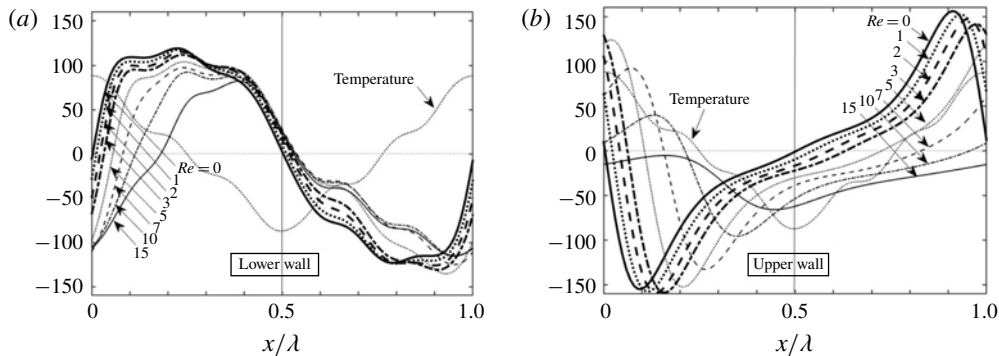
FIGURE 9. Variations of the theoretically determined wall shear at the lower (*a*) and upper (*b*) walls between the hot spots determined for the experimental conditions. The thin dotted lines illustrate the distribution of the lower-wall temperature (not to scale). Here $x = 0$ corresponds to the left-hand hot spot in the observation area.

zone adjacent to the counterclockwise-rotating bubble opposing the fluid movement. The situation at the upper wall is reversed in the sense that shear adjacent to the clockwise-rotating bubble opposes the fluid movement while shear adjacent to the counterclockwise-rotating bubble assists with the fluid movement. This situation is very clear for small Re but becomes more complex with an increase of Re as bubbles decrease in size and their positions shift downstream. The amplitudes of shear variations are very large, especially when compared with the isothermal shear for the upper, $\tau_{U,iso}$, and lower, $\tau_{L,iso}$, walls (see table 2). The largest magnitudes are observed for $Re = 0$ and they decrease with an increase of Re but in a different manner at the upper and lower walls. The maximum at the lower wall starts at around 119 and decreases to 81 when the Reynolds number increases from $Re = 0$ to $Re = 15$, while the minimum starts at around -123 and increases to -115. At the upper wall, the maximum starts at 156 and decreases to -5, while the minimum starts at -115 and increases to -66. Heating always increases the mean shear at the upper wall ($\tau_{U,mean}$) while it decreases the mean shear at the lower wall ($\tau_{L,mean}$). This decrease is always larger resulting in an overall reduction of the shear and, thus, reduction of the pressure gradient (see table 2).

The local values of the wall shear are of the order of 10^{-4} Pa which make them difficult to measure directly (Kahler *et al.* 2012; Dongqing Li 2015). The mean shear is the difference between the integrals of the local shear over its positive segment, where the local shear may reach values of up to 100, and the negative segment, where the local shear may reach values of up to -100 (see figure 9). Accordingly, the local shear must be evaluated very accurately to make the difference between these two integrals meaningful. This shear was determined from the velocity profiles such as those displayed in figure 7.

The experimental velocity data were collected at 37 equally spaced x-locations over one heating wavelength and were utilized in construction of the Chebyshev expansions representing velocity profiles at each location. The expansions were then differentiated analytically to determine velocity derivatives at the walls. This process was tested using theoretically determined u-velocities at the experimental y-locations and the velocity derivatives determined in this manner matched the theoretical derivatives to at least four digits. When the same process is applied to the measured velocities,
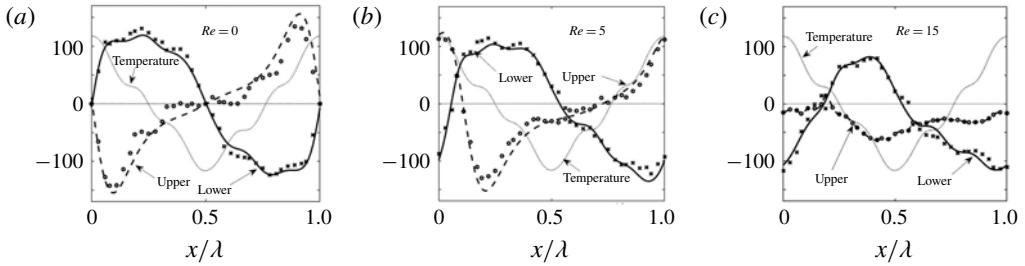
FIGURE 10. Distributions of the wall shear stresses for $Re = 0$ (*a*), $Re = 5$ (*b*) and $Re = 15$ (*c*). Crosses and circles identify experimental points. Thin dotted lines illustrate distributions of the lower-wall temperature (not to scale). Here $x = 0$ corresponds to the left-hand hot spot in the observation area.

it is affected by the measurement error. Results displayed in figure 10 demonstrate that the experimentally determined shear distributions match the theoretical distributions reasonably well in view of the measurement difficulties. The experimental error is however too large to accurately determine the mean shear. The results nevertheless match qualitatively the predicted mean shear and, thus, the predicted pressure gradient reduction. The quantitative differences between the theoretically predicted and the measured pressure gradient reductions are of the order of 100 % and thus are not quoted. The overall character of the experimental data and their qualitative agreement with the theoretical results lead to the conclusion that the experiment does confirm the existence of the pressure-gradient-reducing effect associated with periodic heating. A quantitative confirmation requires the development of either more precise pressure measurement techniques or better velocity measurement techniques in the near-wall regions. Alternatively, a different experimental apparatus could be used. One of the possible alternatives involves reducing the height of the channel to increase pressure losses, but this would lead to challenges with imposing a spatially distributed wall heating. Another alternative is to use low-Prandtl-number fluids as the pressure-gradient-reducing effect is much stronger in such systems (Hossain *et al.* 2012; Floryan & Floryan 2015; Hossain & Floryan 2016).

It is instructive to conclude this discussion with comments about temperature fields and heat fluxes. The theoretical analysis utilizes the Boussinesq approximation which is valid when the temperature differences in the flow system are small. This is an asymptotic statement which does not yield an explicit criterion for determination of the maximum acceptable temperature difference. The excellent agreement between the experimental flow fields and the flow fields of the Boussinesq fluid displayed in figure 6 suggests that the non-Boussinesq effects do not play a major role despite rather large temperature variations existing along the lower wall. Analysis of the temperature fields displayed in figure 6 shows that 'extremely' hot and 'extremely' cold areas occupy a small portion of the overall flow field. The area contained between isotherms $\theta/\theta_{max} = (1, 0.5)$ and $(-1, -0.5)$ shows that the fraction of fluid exposed to extreme temperatures represents less than 5 % of the total volume. The question of non-Boussinesq effects requires further scrutiny with the proper formulation of the field equations given in Frőhlich, Laure & Peyret (1992) and Paolucci (1982).

Analysis of heat transfer provides estimates of energy losses associated with the reduction of the pressure gradient. It is enough to focus on the heat transfer at the
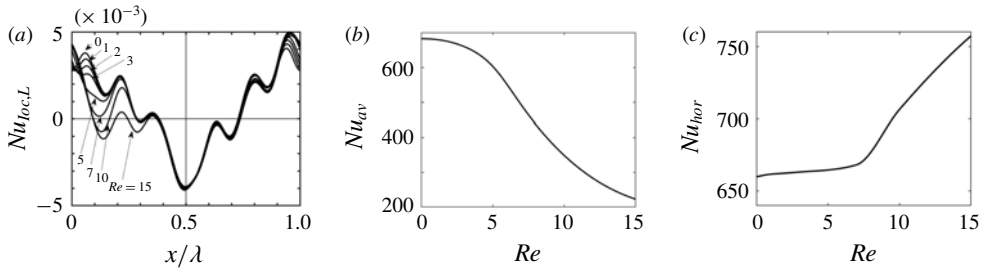
FIGURE 11. (*a*) Distributions of the local Nusselt number at the lower wall $Nu_{loc,L}$. Variations of (*b*) the mean Nusselt number Nu_{mean} and (*c*) the horizontal Nusselt number Nu_{hor} as functions of the Reynolds number.

lower wall. The discussion begins with properties of the local heat flux, the magnitude of which is expressed in terms of the local Nusselt number $Nu_{loc,L}$ defined as

$$Nu_{loc,L} = -\left[\frac{\partial \theta}{\partial y}\right]_{y=-1}. \tag{4.1}$$

Positive values identify areas where the fluid gains energy from the wall while negative values correspond to areas where the fluid loses energy. Increase of *Re* results in a rapid reduction of the magnitude of $Nu_{loc,L}$ near the hot spots while only a marginal change takes place near the cold spots as shown in figure 11(*a*). This explains why the (upstream) separation point moves downstream with increasing *Re* (see figure 6), while the position of the (downstream) attachment point remains nearly unchanged. It may be noted that the direction of the heat flux on the downstream side of the hot spots changes multiple times as *Re* increases.

The net heat flux leaving the lower wall and entering the upper wall, which can be expressed in terms of the average Nusselt number Nu_{av} defined as

$$Nu_{av} = \lambda^{-1} \int_0^\lambda Nu_{loc,L} \, \mathrm{d}x, \tag{4.2}$$

provides one measure of energy losses. Its variations with *Re* illustrated in figure 11(*b*) demonstrate reduction of this loss as *Re* increases, in agreement with Hossain & Floryan (2015*b*).

Temperature variations along the wall are essential for the creation of convection rolls, and their maintenance leads to another cost. This cost consists of thermal conduction along the wall and heat transfer through the fluid between the hot- and cold-wall segments. The former depends on the wall's material and structure and, thus, additional assumptions are needed to determine its magnitude. This problem is outside the scope of the present work. The latter can be quantified in terms of the periodic part of the heat flux leaving the wall. Determination of this heat flux, which we shall refer to as the horizontal heat flux, is complicated as its local direction depends on the Reynolds number (see figure 11*a*). Its magnitude can be measured using the horizontal Nusselt number (Nu_{hor}) defined as

$$Nu_{hor} = \int_L \left[-\frac{\partial \theta}{\partial y} + \frac{\mathrm{d}\mathcal{O}^{(0)}}{\mathrm{d}y}\right]_{y=-1} \mathrm{d}x, \tag{4.3}$$

where L denotes the part of the wall where $Nu_{loc,L} > 0$ and $\emptyset^{(0)}$ stands for mode zero in the numerical representation of the temperature field. Integration over the part of the wall where $Nu_{loc,L} < 0$ produces the same results but with an opposite sign. Results displayed in figure 11(*c*) demonstrate that the 'horizontal heat losses' are always significant; they are nearly constant for $Re < 3$ but begin to increase when $Re \gtrsim 7$.

5. Summary

Analyses of flows in heated horizontal channels were carried out using theoretical and experimental methodologies. A specially designed experimental facility was constructed to realize both well-controlled spatially distributed surface heating and low-Reynolds-number flows with desired flow rates. The theoretical model was generalized to handle experimentally realized heating conditions. The field equations for the Boussinesq fluid were solved with spectral accuracy using Fourier expansions in the streamwise direction and Chebyshev expansions in the wall-normal direction for the heating conditions taken from the experiment.

It was shown that the application of heating in the absence of mean horizontal flow ($Re = 0$) results in the formation of convection rolls whose topology is dictated by the heating wavelength. Addition of a mean pressure gradient results in a competition between the buoyancy-driven and the pressure-gradient-driven flows. When Re is very small, this competition results in the formation of a narrow stream tube winding around the convection rolls and separating clockwise-rotating rolls from direct contact with the upper wall and counterclockwise-rotating rolls from direct contact with the lower wall. Increase of Re leads to the dominance of the pressure-gradient-driven effects leading to an increase of the width of this stream tube and eventual elimination of the rolls. The counterclockwise-rotating rolls are eliminated already at $Re \approx 15$ while the clockwise-rotating roll can be identified until $Re \approx 20$. The change in the flow topology was observed using smoke visualization, PIV measurements as well as theoretical calculations, with the theoretical and experimental results agreeing remarkably well. Velocity measurements provided the means for determination of the wall shear stress. This stress has a spatially periodic distribution with amplitudes two orders of magnitude larger than the isothermal stress. The amplitudes decrease as Re increases but are still very large at $Re = 15$, which is the largest Re used in the experiments. The distributions of shear stresses agree very well with the theoretical predictions.

The theoretical analysis showed that heating leads to a reduction of pressure losses for Reynolds numbers up to $Re \approx 100$. The largest absolute reduction for the heating conditions used in the experiment is achieved for $Re \approx 14$ while the largest relative reduction with respect to the isothermal conditions is achieved for $Re \approx 11$. Limitations of the existing instrumentation prevented the direct measurement of the very small pressure drops for the isothermal as well as non-isothermal conditions. The force-balance approach, where the pressure drop can be predicted from the measured shear forces, proved unsuccessful due to the error accumulation in the evaluation of the local shear stress. Accurate measurements of the flow field provide nevertheless indirect verification of the pressure-gradient-reducing effect as the pressure and velocity fields form a closely coupled system.

REFERENCES

ALJALLIS, E., SARSHAR, M. A., DATLA, R., SIKKA, V., JONES, A. & CHOI, C. H. 2013 Experimental study of skin friction drag reduction on superhydrophobic flat plates in high Reynolds number boundary layer flow. *Phys. Fluids* **25**, 025103.

ARNAL, D., PERRAUD, J. & SÉRAUDIE, A. 2008 Attachment line and surface imperfection problems. In *Advances in Laminar–Turbulent Transition Modeling*, RTO-EN-AVT-151, Brussels, Belgium. Von Karman Institute.

ASAI, M. & FLORYAN, J. M. 2004 Certain aspects of channel entrance flow. *Phys. Fluids* **16**, 1160–1163.

BEWLEY, T. R. 2009 A fundamental limit on the balance of power in a transpiration-controlled channel flow. *J. Fluid Mech.* **632**, 443–446.

BOCQUET, L. & LAUGA, E. 2011 A smooth future? *Nat. Mater.* **10**, 334–337.

DONGQING LI 2015 *Encyclopedia of Microfluidics and Nanofluidics*. Springer.

FLORYAN, D. & FLORYAN, J. M. 2015 Drag reduction in heated channels. *J. Fluid Mech.* **765**, 353–395.

FLORYAN, J. M. 2012 The thermo-superhydrophobic effect. *Bull. Am. Phys. Soc.* **57**, X50.00015.

FLORYAN, J. M., SHADMAN, S. & HOSSAIN, M. Z. 2018 Heating-induced drag reduction in relative movement of parallel plates. *Phys. Rev. Fluids* **3**, 094101.

FRÕHLICH, J., LAURE, P. & PEYRET, R. 1992 Large departures from Boussinesq approximation in the Rayleigh–Bénard problem. *Phys. Fluids* A **4**, 1355–1372.

FUKUNISHI, Y. & EBINA, I. 2001 Active control of boundary-layer transition using a thin actuator. *JSME Intl J.* **44**, 24–29.

HŒPFFNER, J. & FUKAGATA, K. 2009 Pumping or drag reduction? *J. Fluid Mech.* **635**, 171–187.

HOSSAIN, M. Z., FLORYAN, D. & FLORYAN, J. M. 2012 Drag reduction due to spatial thermal modulations. *J. Fluid Mech.* **713**, 398–419.

HOSSAIN, M. Z. & FLORYAN, J. M. 2013a Heat transfer due to natural convection in a periodically heated slot. *Trans. ASME J. Heat Transfer* **135**, 022503.

HOSSAIN, M. Z. & FLORYAN, J. M. 2013b Instabilities of natural convection in a periodically heated layer. *J. Fluid Mech.* **733**, 33–67.

HOSSAIN, M. Z. & FLORYAN, J. M. 2014 Natural convection in a fluid layer periodically heated from above. *Phys. Rev.* E **90**, 023015.

HOSSAIN, M. Z. & FLORYAN, J. M. 2015a Natural convection in a horizontal fluid layer periodically heated from above and below. *Phys. Rev.* E **92**, 023015.

HOSSAIN, M. Z. & FLORYAN, J. M. 2015b Mixed convection in a periodically heated channel. *J. Fluid Mech.* **768**, 51–90.

HOSSAIN, M. Z. & FLORYAN, J. M. 2016 Drag reduction in a thermally modulated channel. *J. Fluid Mech.* **791**, 122–153.

HOSSAIN, M. Z. & FLORYAN, J. M. 2017 Natural convection under sub-critical conditions in the presence of heating non-uniformities. *Intl J. Heat Mass Transfer* **114**, 8–19.

INASAWA, A., NINOMIYA, C. & ASAI, M. 2013 Suppression of tonal trailing-edge noise from an airfoil using a plasma actuator. *AIAA J.* **51**, 1695–1702.

JOSEPH, P., COTTIN-BIZONNE, C., BENOIT, J. M., YBERT, C., JOURNET, C., TABELING, P. & BOCQUET, L. 2006 Slippage of water past superhydrophobic carbon nanotube forests in microchannels. *Phys. Rev. Lett.* **97**, 156104.

KAHLER, J. C., SCHARONOWSKI, S. & CIERPKA, C. 2012 On the uncertainty of digital PIV and PTV near walls. *Exp. Fluids* **52**, 1641–1656.

KATO, T., FUKUNISHI, Y. & KOBAYASHI, R. 1997 Artificial control of the three-dimensionalization process of T–S waves in boundary-layer transition. *JSME Intl J.* **40**, 536–541.

MAMORI, H., IWAMOTO, K. & MURATA, A. 2014 Effect of the parameters of travelling waves created by blowing and suction on the relaminarization phenomena in fully developed turbulent channel flow. *Phys. Fluids* **26**, 015101.

MARTIN, S. & BHUSHAN, B. 2014 Fluid flow analysis of a shark-inspired microstructure. *J. Fluid Mech.* **756**, 5–29.

MIN, T., KANG, S. M., SPEYER, J. L. & KIM, J. 2006 Sustained sub-laminar drag in a fully developed channel flow. *J. Fluid Mech.* **558**, 309–318.

MOHAMMADI, A. & FLORYAN, J. M. 2012 Mechanism of drag generation by surface corrugation. *Phys. Fluids* **24**, 013602.

MOHAMMADI, A. & FLORYAN, J. M. 2013a Pressure losses in grooved channel. *J. Fluid Mech.* **725**, 23–54.

MOHAMMADI, A. & FLORYAN, J. M. 2013b Groove optimization for drag reduction. *Phys. Fluids* **25**, 113601.

MOHAMMADI, A. & FLORYAN, J. M. 2014 Effects of longitudinal grooves on the Couette–Poiseuille flow. *J. Theor. Comput. Fluid Dyn.* **28**, 549–572.

MOHAMMADI, A. & FLORYAN, J. M. 2015 Numerical analysis of laminar-drag-reducing grooves. *Trans. ASME J. Fluids Engng* **137**, 041201.

MOHAMMADI, A., MORADI, H. V. & FLORYAN, J. M. 2015 New instability mode in a grooved channel. *J. Fluid Mech.* **778**, 691–720.

MORADI, H. V. & FLORYAN, J. M. 2013 Flows in annuli with longitudinal grooves. *J. Fluid Mech.* **716**, 280–315.

MORADI, H. V. & FLORYAN, J. M. 2014 Stability of flow in a channel with longitudinal grooves. *J. Fluid Mech.* **757**, 613–648.

OU, J., PEROT, J. B. & ROTHSTEIN, J. P. 2004 Laminar drag reduction in microchannels using ultrahydrophobic surfaces. *Phys. Fluids* **16**, 4635–4643.

OU, J. & ROTHSTEIN, J. P. 2005 Direct velocity measurements of the flow past drag-reducing ultrahydrophobic surfaces. *Phys. Fluids* **17**, 103606.

PAOLUCCI, S. 1982 On the filtering of sound from the Navier–Stokes equations. *Report no.* SAND 82-8257. Sandia National Laboratories.

PARK, H., PARK, H. & KIM, J. 2013 A numerical study of the effects of superhydrophobic surface on skin-friction drag in turbulent channel flow. *Phys. Fluids* **25**, 110815.

PARK, H., SUN, G. & KIM, J. 2014 Superhydrophobic turbulent drag reduction as a function of surface grating parameters. *J. Fluid Mech.* **747**, 722–734.

POETES, R., HOLTZMANN, K., FRANZE, K. & STEINER, U. 2010 Metastable underwater superhydrophobicity. *Phys. Rev. Lett.* **105**, 166104.

QUÉRÉ, D. 2008 Wetting and roughness. *Annu. Rev. Mater. Res.* **38**, 71–99.

RAAYAI-ARDAKANI, S. & MCKINLEY, G. H. 2017 Drag reduction using wrinkled surfaces in high Reynolds number laminar boundary layer flows. *Phys. Fluids* **29**, 093605.

REYSSAT, M., YEOMANS, J. M. & QUÉRÉ, D. 2008 Impalement of fakir drops. *Europhys. Lett.* **81**, 26006.

ROSENBERG, B. J., VAN BUREN, T., FU, M. K. & SMITS, A. J. 2016 Turbulent drag reduction over air- and liquid-impregnated surfaces. *Phys. Fluids* **28**, 015103.

ROTHSTEIN, J. P. 2010 Slip on superhydrophobic surfaces. *Annu. Rev. Fluid Mech.* **42**, 89–109.

SADRI, R. & FLORYAN, J. M. 2002a Accurate evaluation of loss coefficient and entrance length in the inlet region of a channel. *Trans. ASME J. Fluids Engng* **124**, 685–693.

SADRI, R. & FLORYAN, J. M. 2002b Entry flow in a channel. *Comput. Fluids* **31**, 133–157.

SAMAHA, M. A., TAFRESHI, H. V. & GAD-EL-HAK, M. 2011 Modeling drag reduction and meniscus stability of superhydrophobic surfaces comprised of random roughness. *Phys. Fluids* **23**, 012001.

SAMAHA, M. A., TAFRESHI, H. V. & GAD-EL HAK, M. 2012 Influence of flow on longevity of superhydrophobic coatings. *Langmuir* **28**, 9759–9766.

SOLOMON, B. R., KHALIL, K. S. & VARANASI, K. K. 2014 Drag reduction using lubricant-impregnated surfaces in viscous laminar flow. *Langmuir* **30**, 10970–10976.

SOLOMON, B. R., KHALIL, K. S. & VARANASI, K. K. 2016 Correction to drag reduction using lubricant-impregnated surfaces in viscous laminar flow. *Langmuir* **32**, 8287–8287.

SRINIVASAN, S., CHOI, W., PARK, K. C. L., CHHATRE, S. S., COHEN, R. E. & MCKINLEY, G. H. 2013 Drag reduction for viscous laminar flow on spray-coated non-wetting surfaces. *Soft Matt.* **9**, 5691–5702.

SZUMBARSKI, J. 2007 Instability of viscous incompressible flow in a channel with transversely corrugated walls. *J. Theor. Appl. Mech.* **45**, 659–683.

SZUMBARSKI, J., BLONSKI, S. & KOWALEWSKI, T. A. 2011 Impact of transversely-oriented wall corrugation on hydraulic resistance of a channel flow. *Arch. Mech. Engng* **58**, 441–466.

TRUESDELL, R., MAMMOLI, P., VOROBIEFF, P., VAN SWOL, P. & BRINKER, C. J. 2006 Drag reduction on a patterned superhydrophobic surface. *Phys. Rev. Lett.* **97**, 044504.

VAN BUREN, T. & SMITS, A. J. 2017 Substantial drag reduction in turbulent flow using liquid-infused surfaces. *J. Fluid Mech.* **827**, 448–456.

WONG, T. S., KANG, S. H., TANG, S. K. Y., SMYTHE, E. J., HATTON, B. D., GRINTHAL, A. & AIZENBERG, J. 2011 Bioinspired self-repairing slippery surfaces with pressure-stable omniphobicity. *Nature* **477**, 443–447.

YADAV, N., GEPNER, S. W. & SZUMBARSKI, J. 2017 Instability in a channel with grooves parallel to the flow. *Phys. Fluids* **29**, 084104.

YADAV, N., GEPNER, S. W. & SZUMBARSKI, J. 2018 Flow dynamics in longitudinally grooved duct. *Phys. Fluids* **30**, 104105.

ZHOU, M., LI, J., WU, C., ZHOU, X. & CAI, L. 2011 Fluid drag reduction on superhydrophobic surfaces coated with carbon nanotube forest (CNTs). *Soft Matt.* **7**, 4391–4396.